Next Materials 14 (2027) 104056

Contents lists available at ScienceDirect

Next Materials

journal homepage: www.sciencedirect.com/journal/next-materials

Research article

Anisotropic mechanical behavior and oxidation-induced microstructural evolution of Si_3N_4/CNT-graphene hybrid composites

Alaa Almansoori [a,b,*,1], Tamás Kolonits [a,2], Zsolt Czigány [a,3], Katalin Balázsi [a,4], Csaba Balázsi [a,**,5]

[a] Institute for Technical Physics and Materials Science, HUN-REN Centre for Energy Research, Konkoly-Thege Miklós Str. 29-33, Budapest 1121, Hungary
[b] Basrah Engineering Polytechnic College, Southern Technical University, AlZubair Str., Basra 42001, Iraq

ARTICLE INFO

Keywords:
Silicon nitride (Si_3N_4)
CNT–graphene hybrid composites
Powder oxidation
Microstructural evolution
Mechanical anisotropy
Intergranular phases

ABSTRACT

In this study, the effect of Si_3N_4 powder oxidation on the microstructural characteristics and mechanical performance of Si_3N_4/CNT–graphene hybrid composites was investigated using a multiscale approach combining mechanical testing and microstructural characterization. Oxidation resulted in only minor variations in the measured densities, whereas the mechanical properties exhibited a non-monotonic response. Short-term oxidation (10 h) was associated with reduced indentation hardness and modulus, while prolonged oxidation (20 h) resulted in their recovery, particularly on the side surface. Flexural strength increased modestly with oxidation duration. Nanoindentation revealed surface-dependent mechanical behavior, with the side surfaces generally exhibiting higher indentation resistance, consistent with the observed morphology and apparent orientation of elongated β-Si_3N_4 grains. SEM and XRD analyses indicated that the overall grain framework and crystalline phase composition remained essentially unchanged, while surface-dependent differences in grain morphology and relative XRD peak intensities were consistent with preferential grain orientation. HAADF-STEM/EDS analyses revealed an increase in the measured oxygen content, from 10.79 to 16.01 at%, accompanied by broadly comparable spatial distributions of the principal elements, consistent with changes involving the oxygen-containing intergranular regions. These intergranular changes are relevant to grain-boundary interactions, while surface-dependent grain orientation contributes to the observed mechanical anisotropy, although the underlying mechanisms remain to be fully established. These findings provide insights into the structure–property relationships of Si_3N_4/CNT–graphene hybrid composites and highlight the importance of controlling powder oxidation and intergranular phase evolution to tailor their mechanical performance.

1. Introduction

Silicon nitride (Si_3N_4) is a versatile ceramic material that has received great interest in academia and industry owing to its exceptional properties, including its high hardness, good corrosion resistance, proper density, adequate mechanical strength, outstanding thermal stability, and high thermal conductivity [1–3]. In addition, Si_3N_4 withstands high mechanical stress, extreme heat, and corrosive environments, enabling it to maintain its structural integrity and performance even under harsh operating conditions [4,5]. Therefore, this excellent balance of properties makes Si_3N_4 particularly suitable for use in a wide range of applications, including the automotive, aerospace, electronics, and biomedical engineering industries [6–8]. These distinctive properties are associated with its strong covalent bonding

* Corresponding author at: Institute for Technical Physics and Materials Science, HUN-REN Centre for Energy Research, Konkoly-Thege Miklós Str. 29-33, Budapest 1121, Hungary.
** Corresponding author.
E-mail addresses: alaa.almansoori@ek.hun-ren.hu (A. Almansoori), balazsi.csaba@ek.hun-ren.hu (C. Balázsi).
[1] https://orcid.org/0000-0002-9757-7724
[2] https://orcid.org/0000-0002-5836-4398
[3] https://orcid.org/0000-0001-6410-8801
[4] https://orcid.org/0000-0002-8929-9672
[5] https://orcid.org/0000-0003-4219-8783

https://doi.org/10.1016/j.nxmate.2026.104056
Received 28 August 2026; Received in revised form 8 November 2026; Accepted 11 November 2026
Available online 14 November 2026
2949-8228/© 2026 The Authors. Published by Elsevier Ltd. This is an open access article under the CC BY license (http://creativecommons.org/licenses/by/4.0/).

and microstructural characteristics, including the development of elongated β-Si_3N_4 grains during sintering [8]. Furthermore, oxides such as magnesium oxide (MgO), aluminum oxide (Al_2O_3), and yttrium oxide (Y_2O_3) are commonly added to facilitate liquid-phase sintering, promote the α-to-β Si_3N_4 phase transformation and the growth of elongated β-Si_3N_4 grains, and enhance densification [9,10].

Despite these excellent properties and wide applications, certain limitations including machinability, difficulties in producing dense, near-net-shape components, high processing costs, inherent brittleness, and the potential influence of intergranular glassy phases on high-temperature performance, may restrict the broader application of Si_3N_4 ceramics [5,11–14]. To address these challenges, reinforcing materials are typically used to improve the mechanical performance and fracture resistance of ceramic materials, including Si_3N_4, to expand their applications in various engineering sectors. Different types of reinforcements can be employed in ceramic composites in the form of fibers, particles, or whiskers. However, the incorporation of graphene and carbon nanotubes (CNTs) as reinforcing materials has attracted increasing attention due to their exceptional mechanical, thermal, and electrical properties [15–18]. Their distinct structures provide complementary reinforcement mechanisms in ceramic composites. One-dimensional CNTs, characterized by their high aspect ratios and excellent mechanical properties [19], may contribute to fracture resistance through crack bridging and pull-out, whereas two-dimensional graphene, known for its high strength and fracture resistance [20], can provide additional mechanisms, including grain wrapping, anchoring, and crack deflection [21,22]. Accordingly, their combined incorporation into ceramic matrices, including Si_3N_4, may promote complementary toughening mechanisms and improve mechanical performance and fracture resistance [23–25]. Furthermore, hybrid CNT–graphene reinforcement can enhance the electrical conductivity and thermal properties of ceramic composites, expanding their potential applications in multifunctional engineering systems [26,27]. Thus, such composites are attractive for applications that require efficient heat dissipation and high electrical performance, such as thermal management systems, electronics, and structural parts exposed to high thermal and electrical loads [28]. Advanced manufacturing processes, such as hot pressing and spark plasma sintering, can further improve the microstructure of ceramics, resulting in enhanced mechanical performance and reliability [29].

In addition, controlled oxidation of Si_3N_4 powder can modify its surface chemistry through the formation of oxygen-containing species, including silica-rich surface layers, which may influence the subsequent development of intergranular phases during sintering [30–33]. In Si_3N_4 ceramics containing Y_2O_3 and Al_2O_3 sintering aids, these oxygen-containing additives can contribute to the formation of Y–Si–Al–O–N intergranular phases, whose composition and characteristics may influence grain-boundary bonding and crack propagation, thereby affecting mechanical performance [34,35]. Consequently, combining powder oxidation with carbon nanofiller reinforcement may represent a promising strategy for developing multifunctional Si_3N_4 composites with potentially improved mechanical performance and broader engineering applications. Nevertheless, studies investigating the combined effects of Si_3N_4 powder oxidation and hybrid CNT–graphene reinforcement on microstructural development and mechanical performance remain limited. Although previous investigations, including our studies [36,37], have demonstrated the influence of powder oxidation on the microstructural development and mechanical behavior of CNT-reinforced Si_3N_4 composites, these findings cannot be directly extended to hybrid CNT–graphene systems.

Therefore, the potential interactions between oxidation-modified Si_3N_4 powder surfaces and hybrid CNT–graphene reinforcements remain insufficiently understood, particularly regarding their influence on intergranular phase evolution, reinforcement–matrix interactions, and mechanical behavior. Furthermore, the elongated β-Si_3N_4 grain morphology and preferential grain orientation may contribute to orientation-dependent mechanical behavior, particularly at the micro- and nanoscale. Such an anisotropic response has not been systematically explored in Si_3N_4/CNT–graphene composites prepared using oxidized Si_3N_4 powders, despite its potential influence on local deformation mechanisms, interfacial stress transfer, and overall mechanical performance.

Accordingly, this study aims to address these research gaps by investigating the use of oxidized Si_3N_4 powders to develop hybrid Si_3N_4/CNT-graphene nanocomposites. Particular emphasis is placed on the influence of powder oxidation on flexural behavior, the orientation-dependent microstructure of elongated β-Si_3N_4 grains, and its relationship with the anisotropic local mechanical response of the composites. This combined investigation of powder oxidation, hybrid carbon reinforcement, and orientation-dependent mechanical properties represents an additional scientific contribution beyond our earlier studies on CNT-reinforced Si_3N_4 composites.

2. Experimental

2.1. Materials

The raw materials and processing additives used to prepare the Si_3N_4/CNT–graphene composites, incorporating either oxidized or unoxidized Si_3N_4 powders, are described below:

1. The ceramic matrix, alpha-silicon nitride (α-Si_3N_4) powder, was supplied by UBE Corporation (grade SN-ESP).
2. Alumina (Al_2O_3) and yttrium oxide (Y_2O_3) were employed as sintering aids to facilitate densification during sintering. Al_2O_3 was supplied by ALCOA Corporation (grade A16 SG), while Y_2O_3 was supplied by H.C. Starck (C grade).
3. Polyethylene glycol (PEG) was used as an organic additive, serving as a temporary binder during powder processing and shaping.
4. Carbon nanotubes (CNTs) and multilayer graphene were used as hybrid reinforcing materials and supplied by Aldrich.
5. Powder mixtures were processed using an attritor mill (Union Process, type 01-HD/HDDM) equipped with 1 mm diameter zirconia (ZrO_2) grinding media, with ethanol as the milling medium, in a 750 cm^3 zirconia tank.

2.2. Preparation and fabrication

Three batches of α-Si_3N_4 powder were used, one of which remained unoxidized and served as the reference powder, while the other two batches were subjected to oxidation at 1000 °C for 10 and 20 h, respectively. Oxidation was carried out in a furnace under ambient air conditions.

Subsequently, each Si_3N_4 powder batch (90 wt%) was mixed with Al_2O_3 (4 wt%) and Y_2O_3 (6 wt%), followed by the addition of PEG emulsion and ethanol. The mixtures were then milled in an attritor mill with a rotational speed of 4000 rpm for 4.5 h. During the milling process, ZrO_2 particles originating from abrasion of the zirconia grinding media were incorporated into the mixtures. The ZrO_2 content was reported to be within the range of 30–42 wt% [38]. Subsequently, carbon nanotubes (CNTs) and multilayer graphene were added at concentrations of 1 wt% and 2 wt% respectively, and the mixtures were further milled at 600 rpm for 0.5 h.

Following powder preparation, three batches of composite samples (containing unoxidized Si_3N_4, 10 h oxidized Si_3N_4, and 20 h oxidized Si_3N_4, all reinforced with CNTs and graphene) were consolidated using hot isostatic pressing (HIP) at 1700 °C in a nitrogen atmosphere, with a heating rate of 25 °C/min. The gas pressure and holding time were controlled according to the processing conditions specified in Table 1. The dimensions of the sintered samples were 3.5 × 5 × 50 mm. The detailed processing parameters are summarized in Table 1.

Table 1
A detailed description of the starting materials, preparation parameters and sintering process conditions.

i.Preparation of starting powders

Starting powders			Grade/code	Composition (wt%)	Milling process (attritor), Manufacturer: Union Process, Inc.			
					Grinding media	Milling tank	Rotational speed	Time
Matrix	α-Si_3N_4	Unoxidized 10 h oxidized at 1000 °C 20 h oxidized at 1000 °C	SN-ESP	90%	ZrO_2 balls (1 mm diameter)	750 cm^3 ZrO_2 tank	4000 rpm	4.5 h
Sintering aids	Al_2O_3 Y_2O_3		A16-SG C	4% 6%				

ii.Fabrication of composite materials

Sample reference	Sintering powder	Organic additives and solvents	Reinforcement materials	Sintering process (HIP), Manufacturer: ABRA-AG			
				Heating rate	Pressure	Temperature	Holding Time
Unoxidized	Unoxidized powder	PEG and ethanol	1 wt% CNTs and 2 wt% graphene	25 °C/min	20 MPa	1700 °C	3 h
10 h oxidized	10 h oxidized powder	PEG and ethanol	1 wt% CNTs and 2 wt% graphene				
20 h oxidized	20 h oxidized powder	PEG and ethanol	1 wt% CNTs and 2 wt% graphene				

2.3. Testing and measurements

The sintered samples were subjected to mechanical testing and microstructural characterization, as described below, to evaluate the influence of Si_3N_4 powder oxidation on their physical, mechanical and microstructural properties.

1. Density measurement
   The density of sintered samples was measured using the Archimedes method. dry, suspended and saturated weights were measured according to the procedures described in Table S1(i), in supplementary materials, while the equations used to calculate apparent density and bulk densities are presented in Table S1(ii).
2. Microhardness
   Three surfaces of each specimen, namely the top surface and the two side surfaces, were tested for microhardness using a Vickers hardness tester (Litz Wetzlar, Germany) according to BS EN 843–4:2005. On each surface, 12 indentations were performed using a load of 19.61 N and a dwell time of 10 s. Each tested surface was polished prior to testing.
   The mean Vickers hardness (HV) valued were calculated using Equation (1), and the corresponding standard deviations were determined:

$$HV = 1.8544\frac{F}{d^2} \tag{1}$$

   Where F (N) is the applied load, and d (mm) is the mean diagonal length of the indentation.
3. Bending test
   The bending tests were conducted to determine the flexural strength of the sintered samples using a universal testing machine. Two bending test configurations were employed: three-point and four-point bending. In the three-point bending test (3PB), the load was applied at the midpoint between the supports, with a support span length (L) of 20 mm. In the four-point bending test (4PB), the load was applied at two points equidistant from the supports, with a support span length (L) of 40 mm and a distance of 20 mm between the loading points. The flexural strength obtained from the 3PB test was calculated using the following equation:

$$\sigma_{3P} = \frac{3FL}{2bd^2} \tag{2}$$

   For the 4PB test, the flexural strength was calculated using the following equation:

$$\sigma_{3P} = \frac{3FL}{4bd^2} \tag{3}$$

   Where σ_{3p} and σ_{4p} are the flexural strengths obtained from the 3PB and 4PB tests, respectively (MPa), F is the total applied force (N), L is the support span length (mm), b is the width of the specimen (mm), and d is the thickness of the specimen (mm).
4. Scanning electron microscopy (SEM).
   Morphological analysis of the sintered samples was performed using a high-resolution Thermo Fisher Scios 2 DualBeam scanning electron microscope (SEM, Thermo Fisher Scientific, USA). SEM investigations were conducted to examine the shape, apparent orientation, and microstructural characteristics of Si_3N_4 grains, as well as the distribution and homogeneity of the reinforcement materials, namely CNTs and graphene. Qualitative elemental analysis was also performed using energy-dispersive X-ray spectroscopy (EDS) during SEM examination.
5. Transmission electron microscopy (TEM).
   The samples were prepared for TEM examination using Ar ion beam milling at an incident angle of 4° and an accelerating voltage of 10 kV with a Technorg Linda apparatus. The thinning procedure was completed at a reduced ion energy of 3 keV to minimize potential damage from the ion beam. TEM examinations were performed using a Cs-corrected transmission electron microscope (Thermo Fisher Scientific, USA) operated at 200 kV. High-angle annular dark-field (HAADF) images and EDS elemental maps were recorded in scanning transmission electron microscopy (STEM) mode.
6. Nanohardness

Nanohardness was determined to evaluate the resistance of samples to deformation at the nanoscale. An HIT300 nanoindentation tester (Anton Paar TriTec SA, Neuchâtel, Switzerland) was used to measure indentation hardness and elastic modulus at nine different applied loads (1, 2, 5, 10, 20, 50, 100, 200, and 400 mN). At each applied load, 20 indentations were performed on each specimen. Only valid measurements were used to calculate the hardness and elastic modulus values.

3. Results and discussion

3.1. Density results

Three sintered samples from each group(unoxidized, 10 h oxidized, and 20 h oxidized composites) were tested for density measurement, and the results are presented in Table 2. Samples were taken from different locations within the HIP chamber to account for any potential temperature variation during the sintering process.

The apparent density of the unoxidized samples exhibited a relatively wide range (3.181–3.312 g/cm^3), with an average value of 3.246 ± 0.066 g/cm^3 (mean ± SD, n = 3). This variation may be associated with local differences in microstructure, porosity, or sintering conditions, although the present measurements do not allow these contributions to be distinguished. The apparent density showed a decreasing trend with increasing oxidation time, reaching 3.189 ± 0.035 and 3.184 ± 0.025 g/cm^3 for the 10 h and 20 h oxidized samples, respectively. In contrast, the bulk density exhibited a non-monotonic variation, with values of 3.507 ± 0.069, 3.543 ± 0.056, and 3.471 ± 0.042 g/cm^3 for the unoxidized, 10 h, and 20 h oxidized samples, respectively. Overall, these results suggest that controlled powder oxidation was associated with modest changes in the measured densities, with a decreasing trend in apparent density but no corresponding monotonic trend in bulk density. The measured density variations suggest that the influence of powder oxidation on the densification behavior of Si_3N_4/CNT–graphene composites is not straightforward. Although oxidation of the starting Si_3N_4 powder may influence liquid-phase formation and particle bonding during sintering through possible changes in silica-rich intergranular phases, the present density measurements do not demonstrate a consistent improvement in densification with increasing oxidation time. Furthermore, the measured densities may be influenced by the presence and distribution of carbon nanotubes and graphene reinforcements, as well as variations in porosity and intergranular phases.

Pasupuleti et al. [39] and Tatami et al. [40] have reported that incorporating CNT into unoxidized ceramics can reduce their densities to varying degrees depending on CNT content, dispersion quality, and processing conditions. Conversely, some studies have indicated that low CNT content (<4 wt%) or hybrid CNT-graphene structures can enhance the densification of ceramic systems by promoting electrical conductivity and local heating under suitable processing conditions [41,42]. These observations are consistent with our previous research, where low CNT content (3 wt%) enhanced the densification of oxidized Si_3N_4 [37]. However, poor dispersion or agglomeration of hybrid CNT-graphene structures can introduce porosity and hinder densification, leading to lower density values [41].

3.2. Bending and Vickers hardness results

Table 3 presents the results of the bending tests, including 4PB and 3PB tests, performed on three specimens from each material condition. Overall, the obtained results indicate variations in mechanical performance depending on oxidation duration, loading configuration, and measured property. The flexural strengths obtained from the 3PB tests were consistently higher than those obtained from the 4PB tests. This behavior is characteristic of brittle ceramic materials and can be attributed to the larger volume of material subjected to high stresses during the 4PB test, which increases the probability of fracture initiation from critical flaws such as pores, microcracks, and CNT-graphene aggregates.

Oxidation treatment was associated with a gradual increase in average flexural strength in both tests, with the 20 h oxidized composites exhibiting the highest average strength. Specifically, the average flexural strength obtained from 4PB increased from 274.3 MPa for the unoxidized composite to 292.7 MPa after 20 h of oxidation, while the average strength obtained from 3PB increased from 384.7 MPa to 398.0 MPa. As only minor changes in density were observed after oxidation, the observed improvement in flexural strength may not be primarily associated with changes in densification. Instead, it may be related to oxidation-induced modifications in the intergranular phases and grain-boundary characteristics, which could influence crack propagation and the mechanical response of the composites. Crack deflection, bridging, and pull-out associated with the elongated Si_3N_4 grains and carbonaceous reinforcements may also contribute, although their individual contributions were not directly quantified. Furthermore, the coefficient of variation (CV) obtained from 4PB decreased from 9.15% for the unoxidized composites to 2.27% after 10 h of oxidation, suggesting a more consistent flexural response among the tested specimens. Although the 20 h oxidized composites exhibited the highest average strength, the coefficient of variation (CV) increased to 9.33%, suggesting that the increase in strength was not accompanied by a corresponding improvement in the consistency of the measured strength values. Overall, the results indicate that oxidation was associated with changes in both the flexural strength and the variability of the mechanical response of Si_3N_4/CNT-graphene composites.

Similar observations were reported in previous studies, such as those of Pasupuleti et al. [39] and our previous study [43], where the addition of CNT improved the mechanical performance of Si_3N_4 without significantly influencing density. Furthermore, W. Zhao et al. [41] reported that the synergistic combination of graphene and carbon nanotubes promoted grain refinement and improved the mechanical performance of ceramic composites. Overall, the results suggest that powder oxidation is associated with a gradual increase in average flexural strength, while the variability of the measured strength varies with both oxidation duration and bending configuration.

Vickers hardness test results, displayed in Table 4, provide additional insight into the mechanical behavior of Si_3N_4/CNT-graphene composites, revealing a dependence on both oxidation duration and testing surface. For the unoxidized composites, hardness values ranged from 12.64 to 13.77 GPa across the investigated surfaces. This relatively narrow range suggests limited variation in hardness among the investigated surfaces. After oxidation for 10 h, a noticeable decrease in hardness was recorded, especially on the top surface, which exhibited the lowest value of 10.26 GPa. In contrast, the hardness values measured on the two side surfaces showed only minor changes compared with those of the unoxidized composites, ranging from 12.29 to 13.20 GPa. These differences may be associated with local microstructural heterogeneity arising during the sintering process, including variations in grain morphology and orientation, reinforcement distribution, residual porosity, and intergranular phase characteristics. In silicon nitride (Si_3N_4) ceramics, elongated β-Si_3N_4 grains may exhibit different orientations relative to the tested surfaces, influencing local indentation resistance and potentially resulting in measurable differences between surfaces of the same sample.

The composites oxidized for 20 h exhibited the highest hardness values on both side surfaces, reaching 15.69 GPa, while the top surface showed a recovery in hardness compared with the 10 h oxidized composites. This increase suggests that prolonged powder oxidation may have promoted microstructural modifications associated with enhanced resistance to local deformation. Although only minor changes in density were observed, oxidation of the starting Si_3N_4 powder may have altered

Table 2
Density results of Si_3N_4/CNT-graphene composites (Unoxidized, 10 h oxidized, and 20 h oxidized composites).

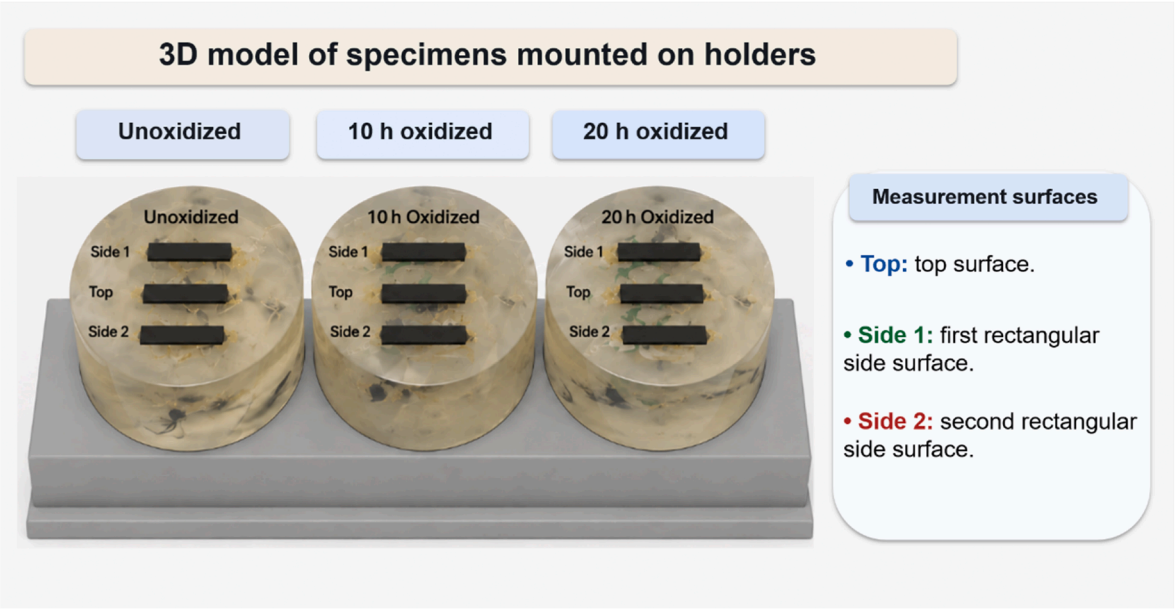
Materials	Apparent density, g/cm^3, mean ± SD	Bulk density, g/cm^3,mean ± SD
Unoxidized	3.246 ± 0.066	3.507 ± 0.069
10 h oxidized	3.189 ± 0.035	3.543 ± 0.056
20 h oxidized	3.184 ± 0.025	3.471 ± 0.042

Table 3
Flexural strength results obtained from three-points (3PB) and four-points (4PB) bending tests of unoxidized, 10 h oxidized, and 20 h oxidized Si_3N_4/CNT-graphene composites.

Materials	4PB results (MPa)	Mean (MPa)	SD (MPa)	CV (%)	3PB results (MPa)	Mean (MPa)	SD (MPa)	CV (%)
Unoxidized	268, 253, 302	274.3	25.1	9.15	381, 386, 387	384.7	3.2	0.84
10 h oxidized	281, 279, 291	283.7	6.4	2.27	365, 419, 376	386.7	28.5	7.38
20 h oxidized	323, 285, 270	292.7	27.3	9.33	424, 390, 380	398	23.1	5.8

Table 4
Vickers hardness results of unoxidized, 10 h oxidized, and 20 h oxidized Si_3N_4/CNT-graphene composites. Inset: 3D model illustrating the three measurement surfaces investigated for each rectangular specimen (Side 1, Top, and Side 2) under the three oxidation conditions. Values are presented as mean ± standard deviation (SD).

Surface	Unoxidized (GPa)	10 h Oxidized (GPa)	20 h Oxidized (GPa)
Side 1	13.63 ± 0.89	13.20 ± 0.74	15.37 ± 1.25
Top	12.64 ± 0.79	10.26 ± 1.45	12.48 ± 1.42
Side 2	13.77 ± 1.65	12.29 ± 0.34	15.69 ± 1.79



the surface chemistry of Si_3N_4 particles, affecting subsequent sintering behavior, grain-boundary development, and interfacial characteristics. Such changes may contribute to improved resistance to deformation beneath the indenter. As discussed earlier, comparable improvements in mechanical properties were recorded without substantial changes in density in Si_3N_4 systems reinforced with either CNTs alone or CNT-graphene hybrid reinforcements, where microstructural characteristics and grain morphology were suggested to contribute to mechanical performance beyond changes in densification. The consistently lower hardness measured on the top surface compared with both side surfaces suggests an orientation-dependent local mechanical response, potentially associated with differences in the morphology and orientation of elongated β-Si_3N_4 grains. The elongated morphology of the β-Si_3N_4 grains and their orientation relative to the indentation direction may influence crack initiation and deformation beneath the indenter, contributing to the observed surface-dependent hardness values [44,45].

Considering the Vickers hardness results across the investigated surfaces, powder oxidation appears to have a non-monotonic influence on the local mechanical response of the composites. Shorter oxidation periods were associated with reduced hardness at certain tested surfaces, while prolonged oxidation was associated with higher hardness and bending strength despite slight changes in density. These results suggest that the observed mechanical behavior may be influenced by microstructural characteristics, grain-boundary evolution, and matrix–reinforcement interactions, in addition to densification.

3.3. Nanoindentation

Fig. 1 presents the load dependent indentation modulus (E_{IT}) and indentation hardness (H_{IT}) of the unoxidized, 10 h, and 20 h oxidized Si_3N_4/CNT–graphene composites, measured on the top and side surfaces. The results are arranged in six panels, with E_{IT} presented in the left column and H_{IT} in the right column, for the three oxidation conditions. Overall, the nanoindentation results indicate that the local mechanical response varies with both oxidation treatment and measurement orientation, where S denotes the side surface and T refers to the top surface. This distinction is important because the two surfaces may expose different cross-sectional orientations of the elongated β-Si_3N_4 grains, potentially influencing their local indentation response.

For the unoxidized composite, both indentation modulus and

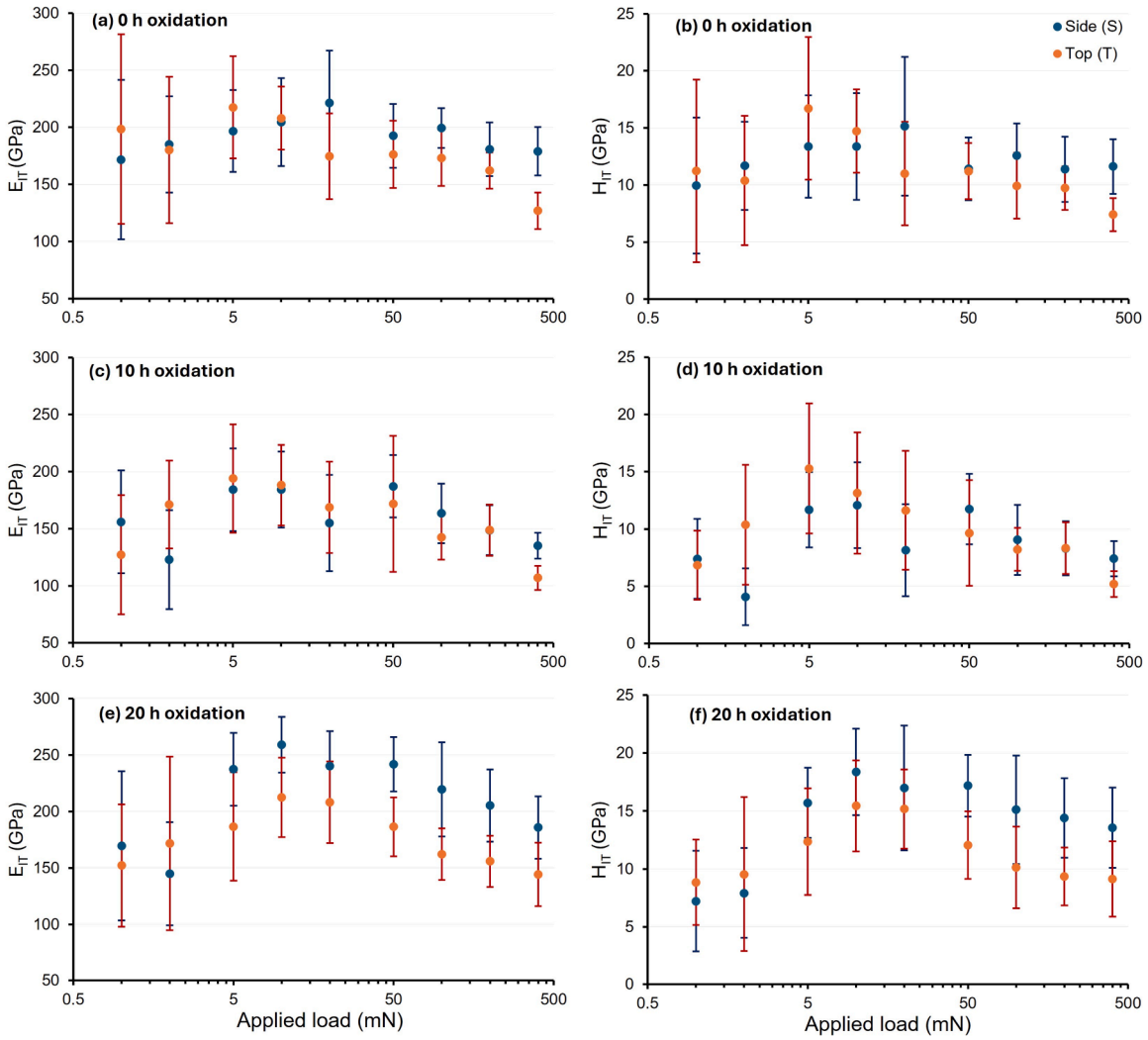


Fig. 1. Load-dependent indentation modulus (E_{IT}) and indentation hardness (H_{IT}) of Si_3N_4/CNT–graphene hybrid composites prepared using unoxidized (a, b), 10 h oxidized (c, d), and 20 h oxidized (e, f) Si_3N_4 powders. Measurements were performed on the side (S) and top (T) surfaces, as identified by the common legend in the upper panels. The applied-load axis shown in the bottom panels is shared by the corresponding panels above. Symbols represent mean values, and error bars indicate standard deviations.

hardness exhibit variations with applied load, reaching relatively high values at intermediate loads, as shown in Figs. 1a and 1b. However, differences are evident between the measurement surfaces. The side surface (S) exhibited higher indentation modulus and hardness than the top surface (T), particularly at higher applied loads, indicating greater local resistance to indentation deformation. This behavior can be attributed to the predominance of axial cross-sections of elongated β-Si_3N_4 grains on the side surface, compared with the more heterogenous grain orientations observed on the top surface, as discussed in the SEM analysis. Such orientation-dependent mechanical behavior has been reported in silicon nitride ceramics, where elongated β-Si_3N_4 grains influence the local mechanical response [46,47]. Furthermore, CNTs and graphene located within the intergranular regions may contribute to local mechanical reinforcement through their interactions with the ceramic matrix, although their individual contributions cannot be distinguished from the present nanoindentation measurements.

After 10 h of oxidation, as shown in Figs. 1c and 1d, both indentation hardness and modulus generally decreased compared with those of the unoxidized composite, although the magnitude of the reduction varied with applied load and measurement surface. The results also exhibited considerable scatter at certain loads, reflecting variations in the local indentation response. These changes suggest that short-term powder oxidation may influence the subsequent development of the intergranular regions during sintering, affecting local deformation resistance. Since oxidation was performed on the Si_3N_4 powder before the incorporation of carbonaceous reinforcements and sintering, the observed differences are more appropriately associated with oxidation-related changes in powder surface chemistry and subsequent microstructural evolution rather than direct oxidation of the sintered composites. After 20 h of oxidation, a substantial recovery in indentation hardness and modulus is evident, particularly on the side surface, where the highest values were observed at intermediate applied loads, as shown in Figs. 1e and 1f. These observations suggest that prolonged powder oxidation may be associated with changes in the intergranular regions that contribute to greater local mechanical resistance, although the extent of improvement depends on the measurement orientation and applied load.

The observed differences between the side and top surfaces should not be interpreted as evidence of oxidation gradients within the sintered samples. Instead, they more likely reflect the microstructural anisotropy associated with the elongated β-Si_3N_4 grains and their orientation relative to the indentation direction. Local variations in the distribution of CNTs, graphene, grain boundaries, and residual porosity may also influence the measured hardness and indentation modulus [44]. The

standard deviation error bars in Fig. 1 further illustrate the variability of the local mechanical response, particularly at lower applied loads, where individual microstructural features may have a greater influence on the indentation measurements. Consequently, nanoindentation provides information about local mechanical heterogeneity, making some variation between measurement locations and specimen surfaces reasonable.

Overall, the nanoindentation results indicate that powder oxidation has a non-monotonic and load-dependent influence on the local mechanical properties of Si_3N_4/CNT–graphene composites. Short-term oxidation (10 h) was associated with reduced indentation hardness and modulus, whereas prolonged oxidation (20 h) promoted a recovery and, particularly on the side surface, an improvement in these properties, despite relatively small changes in overall density. The initial deterioration may be associated with localized changes in the oxygen-containing intergranular phase, potentially affecting grain-boundary bonding and local deformation resistance. Ziegler et al. [48] demonstrated that variations in grain-boundary oxygen content can modify interfacial bonding and fracture behavior in Si_3N_4 ceramics containing Y_2O_3–Al_2O_3 additives. Similarly, Hampshire and Pomeroy [35,49] highlighted the influence of intergranular oxynitride glass composition on mechanical properties and interfacial residual stresses. These findings provide a possible framework for interpreting the oxidation-dependent variations observed in the present composites, although the specific mechanisms cannot be established solely from nanoindentation measurements. Accordingly, the measured response may reflect the combined effects of intergranular phase evolution, reinforcement–matrix interactions, and grain-orientation-dependent mechanical behavior, rather than changes in densification alone [50]. However, the formation of defects, residual stresses, or deterioration of ceramic–carbon interfacial bonding cannot be directly confirmed from the present experimental results.

3.4. SEM investigations

The SEM micrographs of the fracture cross-sections shown in Fig. 2a–f provide insight into the microstructural characteristics of the Si_3N_4/CNT–graphene composites prepared using Si_3N_4 powders subjected to different oxidation durations. In the low-magnification SEM images in Fig. 2a–c, all samples exhibit relatively compact fracture-surface morphologies without extensive cracking or large interconnected porosity, although some localized dark regions are visible. However, slight increases in contrast heterogeneity and localized irregular regions can be observed with increasing powder oxidation time, particularly in the 20 h oxidized sample, suggesting possible changes in the fracture-surface morphology associated with the oxidation treatment of the starting powder.

At higher magnification (Fig. 2d–f), the unoxidized composite shows well-defined angular and elongated Si_3N_4 grains with relatively distinct morphological features, characteristic of a HIP-consolidated Si_3N_4-based microstructure. After 10 h of powder oxidation, localized smoothing of grain edges and minor intergranular modifications appear to be present,

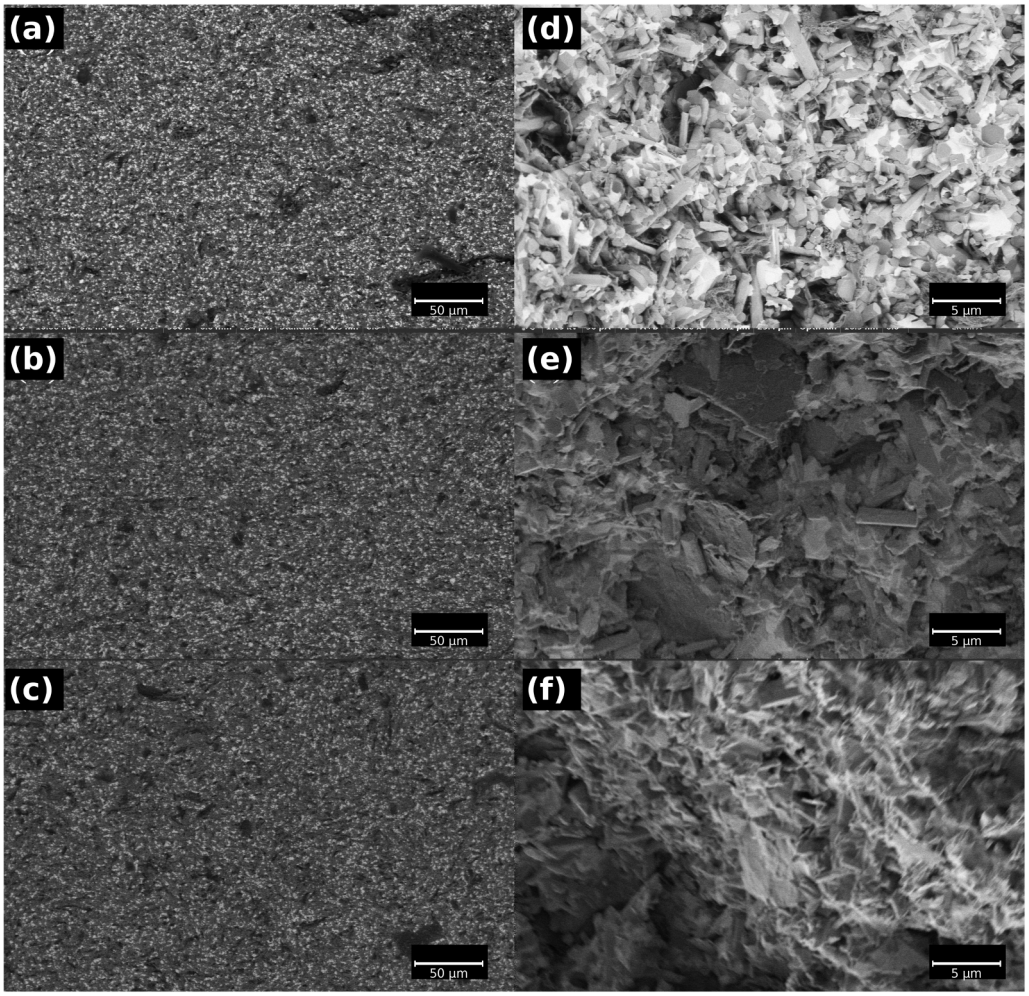


Fig. 2. SEM micrographs of the fracture surfaces of Si_3N_4/CNT–graphene composites at different oxidation durations: (a, d) unoxidized, (b, e) 10 h, and (c, f) 20 h at low and high magnifications.

although their chemical origin cannot be established from SEM morphology alone [51]. Following 20 h of powder oxidation, the fracture surface appears more heterogeneous, with less distinct grain boundaries and irregular fibrous regions distributed across parts of the cross-section. Although a continuous oxide layer cannot be directly resolved, the gradual reduction in grain-boundary definition may reflect changes in the morphology and distribution of grain-boundary regions resulting from the oxidation treatment of the starting Si_3N_4 powder [51]. Importantly, no severe cracking or extensive pore formation is observed across the examined fields, although these observations alone cannot establish the absence of defects throughout the bulk material. Because oxidation was carried out on the Si_3N_4 powder before the incorporation of CNTs and graphene, the observed microstructural differences may be primarily associated with changes in the ceramic matrix and intergranular regions. No obvious degradation of the carbonaceous reinforcements was identified in the examined SEM micrographs, although their structural integrity could not be fully assessed from these observations alone [52,53].

The schematic illustration together with the SEM micrographs in Fig. 3 provides a qualitative representation of the characteristic microstructure of the Si_3N_4/CNT–graphene composites observed from three different orientations, namely, the top surface, side surface, and fracture cross-section. The schematic summarizes the predominant apparent grain orientations and the proposed distribution of the reinforcement phases, whereas the SEM images illustrate the corresponding microstructural features observed experimentally.

The top surface (Fig. 3b) exhibits a relatively compact morphology in which the elongated β-Si_3N_4 grains are only partially distinguishable because many grains appear less clearly exposed than those observed on the side surface. Consequently, the microstructure appears comparatively less directionally defined in the SEM image, with only a limited number of elongated grains directly visible. This observation agrees with the schematic representation, where most elongated grains are intentionally illustrated as being partially hidden beneath the surface. In addition, the intergranular regions appear to occupy a considerable fraction of the exposed surface, suggesting the presence of intergranular phases associated with liquid-phase sintering. This observation is consistent with the characteristic microstructure of liquid-phase-sintered Si_3N_4, where elongated β-Si_3N_4 grains are surrounded by intergranular phases present at grain boundaries and triple junctions [54]. Although individual CNTs and graphene nanoplatelets cannot be clearly resolved in the SEM image because of their nanoscale dimensions and overlap with the ceramic matrix, they may be distributed within these intergranular regions [53].

In contrast, the side surface (Fig. 3c) reveals the anisotropic nature of the β-Si_3N_4 microstructure more clearly. Numerous grains are observed in their axial cross-sections, appearing as polygonal or approximately hexagonal features, while only a limited number of elongated grains are sectioned longitudinally. This morphology suggests that the observation plane intersects many of the elongated β-Si_3N_4 grains approximately perpendicular to their longitudinal axis. Nevertheless, the grain arrangement does not provide conclusive evidence of crystallographic texture, since SEM morphology alone cannot establish the crystallographic orientation distribution [34]. The schematic reproduces this morphology by depicting predominantly axial grain cross-sections together with only a few randomly distributed longitudinal grains, providing a simplified representation of the experimental observations. The fracture surface (Fig. 3d) exhibits a distinctly different morphology owing to crack propagation during mechanical fracture. Unlike the other surfaces, the fracture surface exposes grains from multiple orientations simultaneously, resulting in a heterogeneous mixture of elongated grains, fractured grain segments, and differently oriented grain cross-sections. This morphology may reflect a nonuniform crack path through the composite, potentially involving interactions with elongated β-Si_3N_4 grains and contributing to an irregular fracture topography [34,44].

The schematic illustrates the expected distribution of the principal constituents within the Si_3N_4/CNT–graphene composite. The elongated

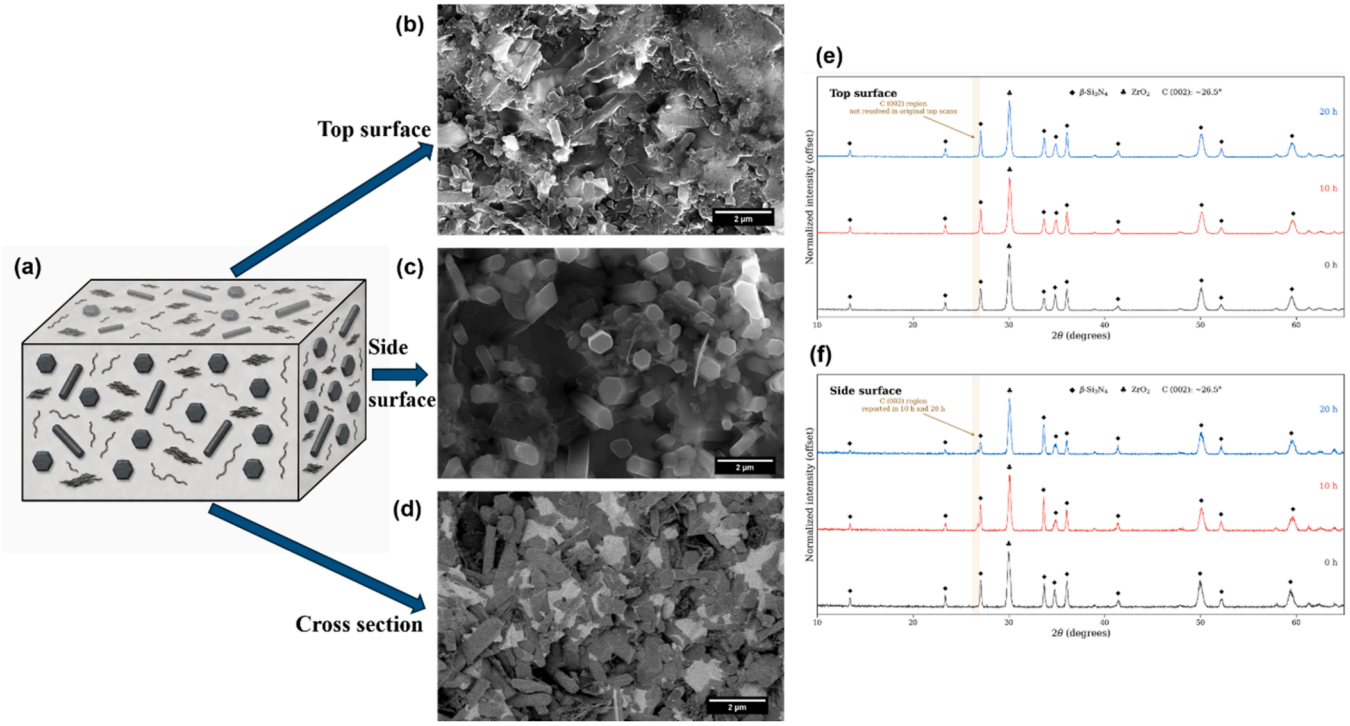


Fig. 3. (a) Schematic representation of the microstructural architecture of the Si_3N_4/CNT–graphene hybrid composite; (b–d) corresponding SEM micrographs of the (b) top surface, (c) side surface, and (d) fracture surface; and (e–f) X-ray diffraction (XRD) patterns obtained from the (e) top and (f) side surfaces of composites prepared using Si_3N_4 powders subjected to different oxidation durations (0 h, 10 h, and 20 h). The diffraction peaks corresponding to β-Si_3N_4 and ZrO_2 are indicated, together with the expected position of the graphite C (002) reflection.

and polygonal features represent the longitudinal and axial sections of β-Si_3N_4 grains, while the intergranular glassy phase, ZrO_2 particles, CNTs, and graphene nanoplatelets are schematically depicted according to their expected locations within the ceramic matrix. Although these fine constituents cannot be individually resolved in the SEM micrographs, their representation is intended to provide a conceptual illustration of the possible constituent arrangement of liquid-phase-sintered Si_3N_4/CNT–graphene composites. The observed microstructural features were broadly similar in their overall grain morphology for the unoxidized and oxidized samples, suggesting that the characteristic Si_3N_4 grain framework was largely retained despite the localized morphological differences observed in Fig. 2.

To complement the microstructural observations presented in Fig. 3a–d and further investigate the crystalline phase composition, X-ray diffraction (XRD) analysis was performed on the unoxidized and oxidized Si_3N_4/CNT–graphene hybrid composites. As shown in Fig. 3e (with an enlarged version provided in Figure S1 of the Supplementary Materials), the diffraction patterns obtained from the top surfaces of all three samples exhibit reflections predominantly associated with β-Si_3N_4 and ZrO_2, with no substantial differences in the detectable crystalline phase assemblage following powder oxidation. Additional XRD measurements performed on the side surfaces (Fig. 3f, with an enlarged version provided in Figure S2 of the Supplementary Materials) revealed a similar crystalline phase assemblage but noticeable differences in the relative intensities of several diffraction reflections compared with those obtained from the top surfaces. In particular, the relative intensity of the β-Si_3N_4 reflection at approximately 33.7° (2θ) was higher on the side surfaces under all three oxidation conditions. These differences are qualitatively consistent with preferential crystallographic orientation of the elongated β-Si_3N_4 grains and complement the surface-dependent grain morphologies observed by SEM.

These observations are consistent with our previous study on Si_3N_4/CNT composites [36], in which β-Si_3N_4 and Y-doped ZrO_2 were identified as the principal crystalline phases, indicating the transformation of α-Si_3N_4 to β-Si_3N_4 during sintering at 1700 °C [55]. The graphite C (002) reflection near 26.5° was not clearly resolved in the top-surface diffraction patterns; however, it was identified in the side-surface patterns of the 10 h and 20 h oxidized samples. This difference indicates surface-dependent detectability of graphitic structures associated with CNT and graphene reinforcements. The enhanced visibility of this reflection on the side surfaces is consistent with possible preferential orientation of the carbonaceous reinforcements, which can influence the relative diffraction intensity of graphitic planes. Furthermore, the absence of clearly resolved crystalline reflections from the sintering additives is consistent with their possible incorporation into an amorphous or poorly crystalline intergranular phase [56]. Therefore, it should be noted that the absence of additional diffraction peaks does not rule out minor secondary phases or oxidation-induced modifications within the intergranular regions and at the carbon-reinforcement interfaces. Given the limited sensitivity of XRD to amorphous or minor phases and the spatial resolution limitations of SEM, further HRTEM and STEM–EDS analyses were employed to better characterize the intergranular phases and carbon-reinforcement interfaces.

3.5. STEM investigations: HAADF images and corresponding EDS elemental maps

The quantitative EDS analyses (Table 5(i-iii)), together with the corresponding HAADF-STEM images and EDS elemental maps (Fig. 4), were employed to investigate the elemental distribution and chemical differences associated with the oxidation treatment of the starting Si_3N_4 powder in the unoxidized, 10 h oxidized, and 20 h oxidized Si_3N_4/CNT–graphene composites. The quantitative EDS results indicate the presence of the principal detected constituent elements, including Si, N, O, Y, Al, and Zr, in all specimens. Most notably, the measured oxygen content increases progressively from 10.79 at% in the unoxidized sample to 13.96 at% after 10 h and 16.01 at% after 20 h of oxidation, whereas the nitrogen content remains relatively stable at 43.92, 44.29, and 42.76 at%, respectively (Table 5(i-iii)). The Si content shows some variation, decreasing from 34.20 at% in the unoxidized sample to 31.12 at% after 10 h and 31.41 at% after 20 h. Similarly, only minor variations are observed in the Y, Al, and Zr contents among the investigated composites. These results suggest that longer powder oxidation durations are associated with higher measured oxygen contents in the analyzed regions in the sintered composites, while the relative proportions of several other detected elements remain broadly comparable.

Table 5
Quantitative EDS elemental composition of the Si_3N_4/CNT–graphene composites prepared using (i) unoxidized, (ii) 10 h oxidized, and (iii) 20 h oxidized Si_3N_4 powders.

i.Unoxidized composite							
Z	**Element**	**Family**	**Atomic Fraction (%)**	**Atomic Error (%)**	**Mass Fraction (%)**	**Mass Error (%)**	**Fit Error (%)**
7	N	K	43.92	3.40	23.26	2.12	5.85
8	O	K	10.79	2.09	6.53	1.34	2.97
13	Al	K	1.75	0.36	1.78	0.37	1.10
14	Si	K	34.20	4.49	36.33	4.67	0.07
39	Y	K	1.56	0.23	5.24	0.76	0.09
40	Zr	K	7.79	1.08	26.86	3.18	0.03
ii.10 h oxidized composite							
Z	**Element**	**Family**	**Atomic Fraction (%)**	**Atomic Error (%)**	**Mass Fraction (%)**	**Mass Error (%)**	**Fit Error (%)**
7	N	K	44.29	3.29	24.15	2.12	5.79
8	O	K	13.96	2.59	8.70	1.73	2.68
13	Al	K	1.80	0.37	1.89	0.39	0.13
14	Si	K	31.12	4.30	34.03	4.53	0.01
39	Y	K	1.41	0.20	4.89	0.70	0.16
40	Zr	K	7.42	1.02	26.86	3.08	0.05
i. **20 h oxidized composite**							
Z	**Element**	**Family**	**Atomic Fraction (%)**	**Atomic Error (%)**	**Mass Fraction (%)**	**Mass Error (%)**	**Fit Error (%)**
7	N	K	42.76	3.25	23.69	2.08	5.55
8	O	K	16.01	2.89	10.13	1.98	1.18
13	Al	K	1.58	0.33	1.68	0.35	1.46
14	Si	K	31.41	4.33	34.89	4.58	0.19
39	Y	K	1.46	0.21	5.12	0.74	0.10
40	Zr	K	6.79	0.95	24.48	2.94	0.11

Overall, the combined HAADF-STEM and EDS results indicate that increasing the oxidation duration of the starting Si_3N_4 powder is associated with higher measured oxygen content in the analyzed regions of the sintered composites, while the characteristic Si_3N_4 grain morphology and the overall distribution of the principal constituent elements remain broadly comparable.

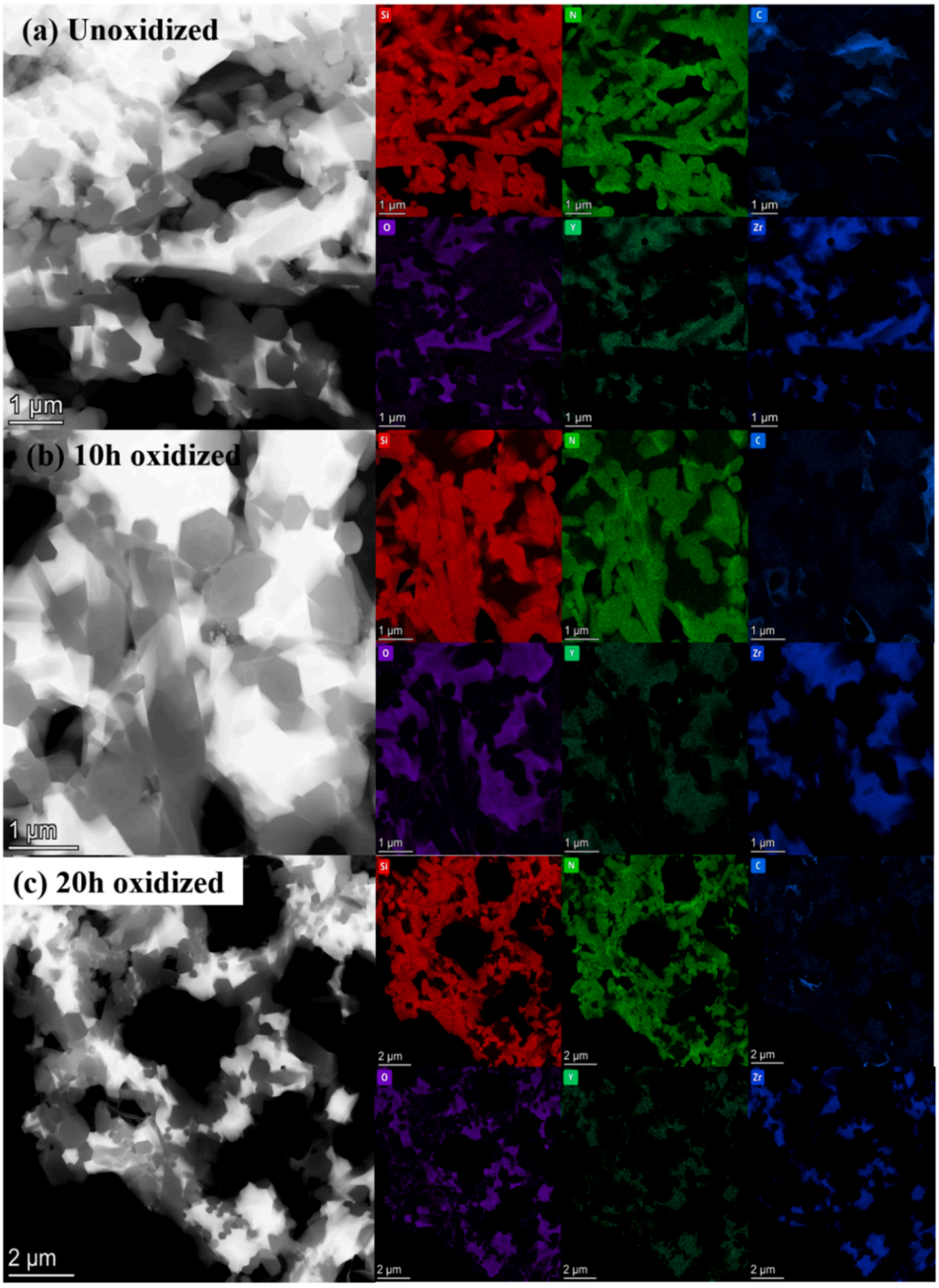


Fig. 4. HAADF-STEM images and corresponding EDS elemental maps showing the spatial distribution of Si, N, C, O, Y, and Zr in Si_3N_4/CNT–graphene composites prepared using (a) unoxidized, (b) 10 h oxidized, and (c) 20 h oxidized Si_3N_4 powders.

The distribution of Y in Fig. 4 and the presence of Al in the elemental maps presented in Fig. 5, together with their limited variation in the quantitative EDS results, are consistent with the presence of Y- and Al-containing intergranular constituents associated with the Y_2O_3–Al_2O_3 sintering additives [57,58].

The corresponding elemental maps (Fig. 4) provide complementary information regarding the spatial distribution of the constituent elements. For the unoxidized composite (Fig. 4a), the Si and N maps exhibit a broad distribution associated with the Si_3N_4-rich regions. The elongated morphology observed in the maps is consistent with the β-Si_3N_4 grains identified by SEM, supporting the presence of an elongated-grain ceramic framework following liquid-phase sintering. Oxygen appears to be distributed heterogeneously, with localized signals that may correspond to oxygen-containing intergranular regions, while the corresponding Y maps show localized elemental signals that may be associated with oxide-derived intergranular constituents, as commonly reported for liquid-phase-sintered Si_3N_4 ceramics [34,44]. The Zr maps further confirm the presence of Zr-containing regions within the examined microstructure, although their distribution is not entirely uniform. Carbon is also detected by EDS; however, because of its relatively low concentration and the limitations of EDS mapping, the elemental maps cannot be used to directly distinguish individual CNTs

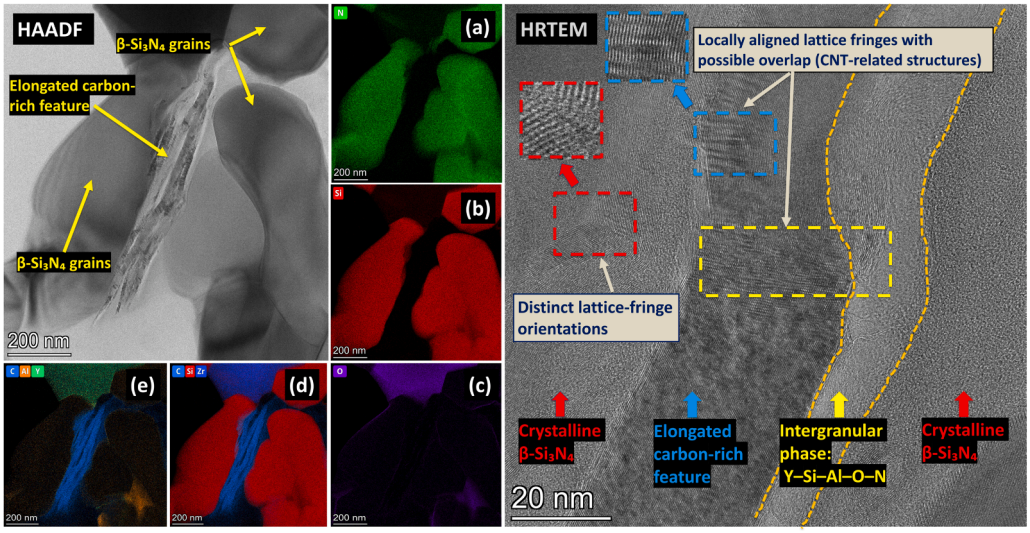


Fig. 5. HAADF-STEM micrograph and corresponding STEM–EDS elemental maps of the Si_3N_4/CNT–graphene hybrid composite prepared using Si_3N_4 powder oxidized for 20 h: (a) N, (b) Si, (c) O, (d) combined C–Si–Zr, and (e) combined C–Al–Y elemental distributions. The HRTEM micrograph (right) highlights crystalline β-Si_3N_4 regions, an elongated carbon-rich feature exhibiting locally aligned and partially intersecting lattice fringes, and an intergranular region.

or graphene nanoplatelets.

Following powder oxidation for 10 h (Fig. 4b), the overall elemental distribution remains broadly comparable to that of the unoxidized composite, whereas the oxygen signal appears more pronounced in some regions, consistent with the higher oxygen content measured by EDS. After 20 h of powder oxidation (Fig. 4c), the quantitative EDS results show a further increase in oxygen content, while the elemental maps retain broadly similar spatial features for the other mapped elements. These observations suggest that the oxidation treatment of the starting powder may influence the oxygen-containing regions formed during subsequent sintering, while the characteristic Si_3N_4 grain morphology remains recognizable, which is consistent with the role of oxygen-containing intergranular phases in liquid-phase-sintered Si_3N_4 ceramics [55]. The persistence of a broadly comparable elemental distribution among the specimens suggests that the principal microstructural constituents remain present despite the increase in measured oxygen content.

More specifically, the increase in measured oxygen content from 13.96 at% after 10 h to 16.01 at% after 20 h of oxidation suggests possible changes in the oxygen-containing intergranular environment. This progressive enrichment may alter the chemical composition of the Y–Si–Al–O–N intergranular glass formed during sintering, potentially affecting its oxygen- and nitrogen-containing network units and associated physicochemical properties. Previous studies have demonstrated that the composition of Si_3N_4 intergranular oxynitride glasses influences their network connectivity, viscosity, and mechanical properties [35,49], while variations in grain-boundary chemistry can affect interfacial bonding and fracture behavior [48]. Changes in glass composition and viscosity may influence the redistribution of the intergranular phase during sintering, whereas the resulting grain-boundary chemistry may affect interfacial cohesion, load transfer, and crack propagation. These effects could contribute to the improved hardness and flexural strength observed after 20 h of oxidation, despite the relatively small changes in density. Nevertheless, the exact intergranular phase composition, viscosity, and interfacial bonding strength were not directly measured; therefore, these mechanisms are proposed as plausible explanations rather than experimentally verified mechanisms.

3.6. Correlation between microstructure and mechanical properties

The combined density, mechanical, nanoindentation, together with SEM, and HAADF-STEM and EDS analyses indicate that the mechanical behavior of the Si_3N_4/CNT–graphene composites is influenced by the combined effects of grain orientation and oxidation-induced evolution of the intergranular phase. The small changes in apparent and bulk densities indicate that oxidation has little influence on overall densification, while SEM and HAADF-STEM/EDS observations suggest that the elongated β-Si_3N_4 grain framework and the distribution of the principal elements are largely preserved. The EDS results also reveal a progressive increase in the measured oxygen content with increasing powder oxidation duration, suggesting possible modifications to the oxygen-containing intergranular regions. These microstructural changes may contribute to the measured mechanical response. The predominance of axial sections of elongated β-Si_3N_4 grains on the side surface could accounts for the higher nanoindentation hardness compared with the top surface. Short-term oxidation (10 h) was associated with reduced hardness and possible localized intergranular modifications, whereas prolonged oxidation (20 h) resulted in improved hardness and flexural strength, potentially influenced by the development of oxygen-enriched intergranular regions. Overall, controlled oxidation for 20 h may improve certain mechanical performance while preserving the fundamental microstructural framework of the composite. Compared with our previous investigations on oxidation-modified Si_3N_4/CNT composites [36,37], the present study provides additional insights into the mechanical behavior of hybrid CNT–graphene-reinforced Si_3N_4. In particular, the combined evaluation of flexural properties, orientation-dependent β-Si_3N_4 grain morphology, and local mechanical response highlights the importance of both intergranular phase evolution and microstructural anisotropy in understanding the effects of powder oxidation. These findings extend the scope of our previous studies by providing a more comprehensive understanding of the relationship between oxidation-induced microstructural modifications and the mechanical behavior of the hybrid composite system.

Further HAADF-STEM, elemental mapping, and HRTEM analyses of the composite prepared using Si_3N_4 powder oxidized for 20 h provide additional insight into the intergranular regions and carbon-reinforcement interfaces (Fig. 5). The elemental maps reveal an elongated carbon-rich feature between β-Si_3N_4 grains, while HRTEM observations show locally aligned and partially intersecting lattice fringes, potentially associated with CNT-related graphitic structures. These observations are consistent with our previous investigation of Si_3N_4/CNT composites [36], which highlighted the influence of powder oxidation on the interfacial characteristics of CNT-reinforced ceramics. Furthermore, a region of comparatively weak lattice ordering near the

carbon-rich feature suggests the possible presence of an amorphous intergranular phase. The observed arrangement of carbon-rich features, crystalline grains, and intergranular regions may influence interfacial load transfer and crack propagation, thereby contributing to the mechanical response of the hybrid composites. The original, unannotated HRTEM image is provided in Figure S3 (Supplementary Materials).

In addition to the effects of grain orientation and intergranular phase evolution, the hybrid CNT–graphene reinforcements may contribute to the mechanical response through their interactions with the oxidation-modified ceramic matrix. Since Si_3N_4 powder oxidation was performed before introducing the carbon nanofillers, the resulting oxygen-containing surface species may influence the subsequent formation of intergranular phases and their interactions with CNTs and graphene during sintering. Compared with CNT-only reinforcement, the incorporation of graphene introduces additional two-dimensional interfaces that may influence grain-boundary interactions and crack propagation through complementary mechanisms, including crack bridging, pull-out, and crack deflection. Furthermore, Zhao et al. [41] reported that interconnected CNT–graphene networks can enhance thermal transport and influence grain-boundary diffusion and grain growth during ceramic sintering, potentially modifying the resulting microstructure. In the present composites, these possible interactions could contribute to the observed variations in mechanical properties with oxidation duration. However, the relatively small density changes and preservation of the elongated β-Si_3N_4 grain framework do not provide direct evidence of enhanced densification or grain refinement. Therefore, the individual contributions of CNTs and graphene and their potential synergistic effects cannot be conclusively distinguished from the present results.

4. Conclusions

This study investigated the influence of Si_3N_4 powder oxidation duration on the microstructure and mechanical performance of Si_3N_4/CNT–graphene composites using density measurements, SEM, HAADF-STEM/EDS, Vickers hardness, bending strength, and nanoindentation. Oxidation was associated with variations in the measured densities, while the characteristic elongated β-Si_3N_4 grain framework remained largely preserved. SEM and HAADF-STEM imaging, together with EDS elemental analyses, further revealed localized morphological differences and an increase in the measured oxygen content with longer powder oxidation durations, while the overall distributions of the principal constituent elements remained broadly comparable.

The mechanical properties exhibited different trends with increasing powder oxidation duration. Short-term oxidation (10 h) was associated with reduced hardness at certain measurement surfaces and applied loads and variations in the mechanical response, whereas prolonged oxidation (20 h) was associated with higher Vickers hardness on both side surfaces, recovery in nanoindentation hardness and indentation modulus, and increased average bending strength. These improvements may be related to changes in intergranular phase characteristics and grain-boundary morphology. However, the precise contributions of intergranular phase evolution and grain-boundary interactions to the mechanical response remain to be fully established. The higher nanoindentation hardness measured on the side surface was potentially related to the predominance of axial cross-sections of elongated β-Si_3N_4 grains, highlighting the possible influence of microstructural anisotropy on localized deformation.

Overall, controlled oxidation of the Si_3N_4 powder prior to sintering shows potential as a pretreatment for modifying the intergranular microstructure and mechanical performance of the resulting Si_3N_4/CNT–graphene composites. The findings suggest that selecting appropriate powder oxidation conditions offers a practical approach to adjusting the mechanical response of Si_3N_4-based hybrid composites while retaining their characteristic elongated-grain microstructure.

Declaration of Generative AI and AI-assisted technologies in the writing process

During the preparation of this manuscript, the authors used ChatGPT (OpenAI) to assist with content organization, grammatical corrections, and improvements in the clarity and readability of the text. The authors reviewed and edited the AI-assisted content and take full responsibility for the accuracy, originality, and scientific integrity of the published work.

Declaration of Competing Interest

The authors declare that they have no known competing financial interests or personal relationships that could have appeared to influence the work reported in this paper.

Acknowledgement

The authors thank Mr. V. Varga for sample preparation. This work was supported by the National Research, Development, and Innovation Office (Hungary)–OTKA NKFI 146076. The Transmission Electron Microscopy (TEM) facility was also supported by grant no. VEKOP-2.3.3–15–2016–00002 of the European Structural and Investment Funds (Hungary). The paper is partially supported by Southern Technical University under scientific research awards, No. 9/7934,10 Sep. 2025.

Appendix A. Supporting information

Supplementary data associated with this article can be found in the online version at doi:10.1016/j.nxmate.2026.104056.

References

[1] B. Zhao, I. Khader, R. Raga, U. Degenhardt, A. Kailer, Tribological behavior of three silicon nitride ceramics in dry sliding contact against Inconel 718 over a wide range of velocities, Wear 448449 (2020) 203206, https://doi.org/10.1016/j.wear.2020.203206.
[2] Y. Wang, et al., Thermal and mechanical properties of Si3N4 ceramics obtained via two-step sintering, Ceram. Int. 48 (13) (2022) 18294–18301, https://doi.org/10.1016/j.ceramint.2022.03.088.
[3] F. Hu, Z.P. Xie, J. Zhang, Z.L. Hu, D. An, Promising high-thermal-conductivity substrate material for high-power electronic device: silicon nitride ceramics, Rare Met. 39 (5) (2020) 463–478, https://doi.org/10.1007/s12598-020-01376-7.
[4] Z. Krstic, V.D. Krstic, Silicon nitride: The engineering material of the future, J. Mater. Sci. 47 (2012) 535–552, https://doi.org/10.1007/s10853-011-5942-5.
[5] M.H. Bocanegra-Bernal, B. Matovic, Mechanical properties of silicon nitride-based ceramics and its use in structural applications at high temperatures, Materials Science Engineering A 527 (6) (2010) 1314–1338, https://doi.org/10.1016/j.msea.2009.09.064.
[6] D.A. Taher, M.A. Hameed, Structural and Hardness Characteristics of Silicon Nitride Thin Films Deposited on Metallic Substrates by DC Reactive Sputtering Technique, Silicon 15 (18) (2023) 7855–7864, https://doi.org/10.1007/s12633-023-02604-2.
[7] X. Xu, et al., New strategies for preparing nanosized silicon nitride ceramics, J. Am. Ceram. Soc. 88 (4) (2005) 934–937, https://doi.org/10.1111/j.1551-2916.2005.00187.x.
[8] G. hua Peng, X. guo Li, M. Liang, Z. hua Liang, Q. Liu, W. lan Li, Spark plasma sintered high hardness α/β Si3N4 composites with MgSiN2 as additives, Scr. Mater. 61 (4) (2009) 347–350, https://doi.org/10.1016/j.scriptamat.2009.04.007.
[9] L. He, N. Huang, D. Lu, P. Sheng, W. Zou, A Study on the Effects of Liquid Phase Formation Temperature and the Content of Sintering Aids on the Sintering of Silicon Nitride Ceramics, Crystals 13 (7) (2023), https://doi.org/10.3390/cryst13071099.
[10] Y. Li, et al., Microstructure and thermal conductivity of gas-pressure-sintered Si3N4 ceramic: the effects of Y2O3 additive content, J. Eur. Ceram. Soc. 41 (1) (2021) 274–283, https://doi.org/10.1016/j.jeurceramsoc.2020.08.035.
[11] M.H. Bocanegra-Bernal, B. Matovic, Dense and near-net-shape fabrication of Si3N4 ceramics, Materials Science Engineering A 500 (1–2) (2009) 130–149, https://doi.org/10.1016/j.msea.2008.09.015.
[12] P.F. Becher, S.-L. Hwang, C.-H. Hsueh, Using Microstructure to Attack the Brittle Nature of Silicon Nitride Ceramics, MRS Bull. 20 (1995) 23–27, https://doi.org/10.1557/S0883769400049174.
[13] C. Montanari, 'Additive Manufacturing of Silicon Nitride', Luleå University of Technology, Gothenburg, 2017, https://www.diva-portal.org/smash/get/diva2:1107442/FULLTEXT01.pdf (accessed 18 January 2026).

[14] A.B. Peters, et al., Selective laser reaction synthesis of SiC, Si_3N_4 and HfC/SiC composites for additive manufacturing, J. Eur. Ceram. Soc. 43 (4) (2023) 1270–1283, https://doi.org/10.1016/j.jeurceramsoc.2022.11.015.

[15] C. Balázsi, et al., Development of CNT/Si3N4 composites with improved mechanical and electrical properties, ' Compos. B Eng. 37 (6) (2006) 418–424, https://doi.org/10.1016/j.compositesb.2006.02.006.

[16] A. Qadir, S. Ali, J. Dusza, D. Rafaja, Predicting hardness of graphene-added Si3N4 using machine learning: A data-driven approach, Open. Ceram. 19 (2024) 100634, https://doi.org/10.1016/j.oceram.2024.100634.

[17] O. Tapasztó, et al., Highly wear-resistant and low-friction Si3N4 composites by addition of graphene nanoplatelets approaching the 2D limit, Sci. Rep. 7 (1) (2017) 1–8, https://doi.org/10.1038/s41598-017-10290-5.

[18] P. Hvizdoš, V. Puchý, A. Duszová, J. Dusza, C. Balázsi, Tribological and electrical properties of ceramic matrix composites with carbon nanotubes, Ceram. Int. 38 (7) (2012) 5669–5676, https://doi.org/10.1016/j.ceramint.2012.04.010.

[19] M. Wiśniewska, et al., Influence of carbon nanotubes on thermal and electrical conductivity of zirconia-based composite, Ceram. Int. 49 (10) (2023) 15442–15450, https://doi.org/10.1016/j.ceramint.2023.01.129.

[20] P. Zhang, et al., Fracture toughness of graphene, Nat. Commun. 5 (2014), https://doi.org/10.1038/ncomms4782.

[21] D. Sun, et al., Fabrication and mechanical properties of Al2O3–TiC ceramic composites synergistically reinforced with multi-walled carbon nanotubes and graphene nanoplates, Ceram. Int. 46 (12) (2020) 20068–20080, https://doi.org/10.1016/j.ceramint.2020.05.081.

[22] B. Yazdani, Y. Xia, I. Ahmad, Y. Zhu, Graphene and carbon nanotube (GNT)-reinforced alumina nanocomposites, J. Eur. Ceram. Soc. 35 (1) (2015) 179–186, https://doi.org/10.1016/j.jeurceramsoc.2014.08.043.

[23] K. Balázsi, M. Furkó, C. Balázsi, Ceramic Matrix Graphene and Carbon Nanotube Composites, Encycl. Mater. Tech. Ceram. Glass. Vol. 1-3 2 (2021) 243–259, https://doi.org/10.1016/B978-0-12-818542-1.00070-9.

[24] K. Balázsi, A. Almansoori, C. Balázsi, Superior Ceramics: Graphene and Carbon Nanotube (CNT) Reinforcements, Ceramics 7 (4) (2024) 1758–1778, https://doi.org/10.3390/ceramics7040112.

[25] A. Almansoori, K. Balázsi, C. Balázsi, Advances, Challenges, and Applications of Graphene and Carbon Nanotube-Reinforced Engineering Ceramics, Nanomaterials 14 (23) (2024), https://doi.org/10.3390/nano14231881.

[26] J.H. Shin, J. Choi, M. Kim, S.H. Hong, Comparative study on carbon nanotube- and reduced graphene oxide-reinforced alumina ceramic composites, Ceram. Int. 44 (7) (2018) 8350–8357, https://doi.org/10.1016/j.ceramint.2018.02.024.

[27] M. Rouway, Z. Boulahia, N. Chakhchaoui, O. Cherkaoui, L.H. Omari, F. Fraija, Graphene and carbone nanotubes reinforced ceramic nanocomposite TiO_2-MgO: Experimental and numerical study, Mater. Today Proc. 30 (2019) 809–815, https://doi.org/10.1016/j.matpr.2020.04.177.

[28] R. Sharma, K.K. Kar, Carbon Nanotube-/Graphene-Reinforced Ceramic Composites, in: K.K. Kar (Ed.), Composite Materials, Springer Berlin Heidelberg, Berlin, Heidelberg, 2017, pp. 599–625, https://doi.org/10.1007/978-3-662-49514-8_17.

[29] C. Balázsi, et al., Processing of carbon nanotube reinforced silicon nitride composites by spark plasma sintering', Compos. Sci. Technol. 65 (5) (2005) 727–733, https://doi.org/10.1016/j.compscitech.2004.10.006.

[30] H. Liang, Y. Zeng, K. Zuo, X. Xia, D. Yao, J. Yin, The effect of oxidation on the mechanical properties and dielectric properties of porous Si3N4 ceramics, Ceram. Int. 43 (7) (2017) 5517–5523, https://doi.org/10.1016/j.ceramint.2017.01.074.

[31] C. He, L. Wang, J. Wu, Oxidation of sintered silicon nitride - Part II Mechanical properties, J. Mater. Sci. 28 (18) (1993) 4829–4834, https://doi.org/10.1007/BF00361142.

[32] S. Natansohn, A.E. Pasto, W.J. Rourke, Effect of Powder Surface Modifications on the Properties of Silicon Nitride Ceramics, J. Am. Ceram. Soc. 76 (9) (1993) 2273–2284, https://doi.org/10.1111/j.1151-2916.1993.tb07764.x.

[33] J. Gubicza, P. Arató, F. Wéber, A. Juhász, Mechanical properties of oxidized silicon nitride ceramics, Materials Science Engineering A 259 (1) (1999) 65–72, https://doi.org/10.1016/S0921-5093(98)00870-3.

[34] S. Hampshire, Silicon nitride ceramics-review of structure, processing and properties', J. Achiev. Mater. Manuf. Eng. 24 (1) (2007) 43–50.

[35] S. Hampshire, M.J. Pomeroy, 'Silicon nitride - Grain boundary oxynitride glass interfaces: Deductions from glass bulk properties, Int. J. Appl. Ceram. Technol. 10 (5) (2013) 747–755, https://doi.org/10.1111/ijac.12136.

[36] A. Almansoori, A.S. Rácz, Z. Czigány, K. Balázsi, C. Balázsi, Effect of Silicon Nitride (Si3N4) Powder Oxidation on the Microstructural and Interfacial Characteristics of Carbon Nanotube (CNT)-Reinforced Si3N4 Ceramics (Part C), Ceram. Int. 51 (30) (2025) 65592–65599, https://doi.org/10.1016/j.ceramint.2025.11.236.

[37] A. Almansoori, T. Kolonits, W. Alkaron, K. Balázsi, C. Balázsi, Tuning the microstructural and micro-/nanomechanical properties of silicon nitride–carbon nanotube composites by powder oxidation, Int. J. Appl. Ceram. Technol. 23 (1) (2026), https://doi.org/10.1111/ijac.70064.

[38] Z. Liao, et al., Microstructure and fracture mechanism investigation of porous silicon nitride–zirconia–graphene composite using multi-scale and in-situ microscopy, Nanomaterials 11 (2) (2021) 1–13, https://doi.org/10.3390/nano11020285.

[39] S. Pasupuleti, et al., Toughening behavior in a carbon nanotube reinforced silicon nitride composite, Materials Science Engineering A 491 (1–2) (2008) 224–229, https://doi.org/10.1016/j.msea.2008.04.058.

[40] J. Tatami, T. Katashima, K. Komeya, T. Meguro, T. Wakihara, Electrically conductive CNT-dispersed silicon nitride ceramics, J. Am. Ceram. Soc. 88 (10) (2005) 2889–2893, https://doi.org/10.1111/j.1551-2916.2005.00539.x.

[41] W. Zhao, J. Sun, Z. Huang, Three-dimensional graphene-carbon nanotube reinforced ceramics and computer simulation, Ceram. Int. 47 (24) (2021) 33941–33955, https://doi.org/10.1016/j.ceramint.2021.08.304.

[42] D. Wei, et al., Effects of carbon nanotubes on densification, microstructure and mechanical properties of boron carbide composite ceramics, J. Alloy. Compd. 1058 (2026) 187035, https://doi.org/10.1016/j.jallcom.2026.187035.

[43] C. Balázsi, Z. Kónya, F. Wéber, L.P. Biró, and P. Arató, 'Preparation and characterization of carbon nanotube reinforced silicon nitride composites', *Materials Science and Engineering C* 23 (6–8) (203) 1133–1137, https://doi.org/10.1016/j.msec.2003.09.085.

[44] X. Zhu, Y. Sakka, Textured silicon nitride: processing and anisotropic properties, Sci. Technol. Adv. Mater. 9 (3) (2008) 033001, https://doi.org/10.1088/1468-6996/9/3/033001.

[45] M.J. Hohann, G. Petzow, Tailored microstructures of silicon nitride ceramics', Pure Appl. Chem. 66 (9) (1994) 1807–1814, https://doi.org/10.1351/pac199466091807.

[46] M. Mitomo, N. Hirosaki, T. Nishimura, R.-J. Xie, Microstructure Control in Silicon Nitride Ceramics-A Review, J. Ceram. Soc. Jpn. 114 (1335) (2006) 867–872, https://doi.org/10.2109/jcersj.114.867.

[47] K. HIRAO, Microstructure Control of Silicon Nitride Ceramics by Seeding and their Enhanced Mechanical and Thermal Properties, J. Ceram. Soc. Jpn. 114 (1332) (2006) 665–671, https://doi.org/10.2109/jcersj.114.665.

[48] A. Ziegler, J.M. McNaney, M.J. Hoffmann, and R.O. Ritchie, 'On the effect of local grain-boundary chemistry on the macroscopic mechanical properties of a high-purity Y 2O 3-Al 2O 3-containing silicon nitride ceramic: Role of oxygen', *Journal of the American Ceramic Society* 88 (7) 1900–1908, https://doi.org/10.1111/j.1551-2916.2005.00412.x.

[49] S. Hampshire, M.J. Pomeroy, Grain boundary glasses in silicon nitride: A review of chemistry, properties and crystallisation, J. Eur. Ceram. Soc. 32 (9) (2012) 1925–1932, https://doi.org/10.1016/j.jeurceramsoc.2011.12.023.

[50] Y.-H. Koh, H.-W. Kim, H.-E. Kim, Mechanical Properties and Oxidation Resistance of Si_3N_4-SiC Nanocomposites, Scr. Mater. 44 (8-9) (2001) 2069–2073, https://doi.org/10.1016/S1359-6462(01)00885-5.

[51] P. Andrews, F.L. Riley, The Microstructure and Composition of Oxide Films Formed during High Temperature Oxidation of a Sintered Silicon Nitride, J. Eur. Ceram. Soc. 5 (4) (1989) 245–256, https://doi.org/10.1016/S0955-2219(89)80008-1.

[52] S.-M. Han, S.-M. Lee, S.-J.L. Kang, Phase transformation and microstructure development in silicon nitride based materials. Advanced Materials '93, Elsevier, 1994, pp. 851–856, https://doi.org/10.1016/B978-0-444-81991-8.50205-3.

[53] A. Qadir, K. Balazsi, C. Balazsi, M. Ivor, J. Dusza, Properties of MWCNTs added Si3N4 composites processed from oxidized silicon nitride powders, Process. Appl. Ceram. 14 (1) (2020) 25–31, https://doi.org/10.2298/PAC2001025Q.

[54] J.-F. Yang, T. Ohji, S. Kanzaki, A. Díaz, S. Hampshire, Microstructure and Mechanical Properties of Silicon Nitride Ceramics with Controlled Porosity, J. Am. Ceram. Soc. 85 (6) (2002) 1512–1516, https://doi.org/10.1111/j.1151-2916.2002.tb00305.x.

[55] A. Qadir, Z. Fogarassy, Z.E. Horváth, K. Balazsi, C. Balazsi, Effect of the oxidization of Si3N4 powder on the microstructural and mechanical properties of hot isostatic pressed silicon nitride, Ceram. Int. 44 (12) (2018) 14601–14609, https://doi.org/10.1016/j.ceramint.2018.05.081.

[56] D. Hou, Y. Han, J. Nie, Y. Zhang, L. Chen, Effect of Y2O3-Al2O3 Additives on the Microstructure and Electrical Properties Evolution of Si3N4 Ceramics, Appl. Sci. 14 (3) (2024), https://doi.org/10.3390/app14031125.

[57] Y. Han, et al., Enhanced mechanical properties and in vitro bioactivity of silicon nitride ceramics with SiO_2, Y_2O_3, and Al_2O_3 as sintering aids, J. Mech. Behav. Biomed. Mater. 164 (2025) 106901, https://doi.org/10.1016/j.jmbbm.2025.106901.

[58] J.-F. Yang, T. Ohji, K. Niihara, Influence of Yttria-Alumina Content on Sintering Behavior and Microstructure of Silicon Nitride Ceramics, J. Am. Ceram. Soc. 83 (8) (2000) 2094–2096, https://doi.org/10.1111/j.1151-2916.2000.tb01520.x.